Advances in Science and Technology Research Journal

Advances in Science and Technology Research Journal, 2025, 19(4), 386–400
https://doi.org/10.12913/22998624/200867
ISSN 2299-8624, License CC-BY 4.0

Received: 2024.11.28
Accepted: 2025.01.25
Published: 2025.02.19

Analysis of the turbulence field in a low-speed fan test rig with distorted inflow

Adam Sieradzki[1*], Tomasz Kwiatkowski[1], Grzegorz Krysztofiak[1], Paweł Ruchała[1], Borys Łukasik[2], Mark Turner[3]

[1] Department of Aerodynamics, Łukasiewicz Research Network, Institute of Aviation, Warsaw, Poland
[2] Department of Aircraft Propulsion, Łukasiewicz Research Network, Institute of Aviation, Warsaw, Poland
[3] Department of Aerospace Engineering, University of Cincinnati, Cincinnati, Ohio, USA
* Corresponding author's e-mail: adam.sieradzki@ilot.lukasiewicz.gov.pl

ABSTRACT

Boundary layer ingestion (BLI) fans demonstrate significant potential for reducing fuel consumption in aircraft propulsion. However, BLI introduces an augmented and uneven turbulence intensity profile at the engine inlet, a factor that can significantly influence turbomachinery performance. This paper aims to analyze the turbulence field within a low-speed fan test rig replicating BLI conditions. Inflow distortion was induced using a variable porosity screen, and turbulence intensity was measured using a hot-wire anemometer mounted on an automated traverse system. The paper presents experimental results obtained at various cross-sections of the rig – upstream, downstream, and between the rotor and the stator. Diverse data processing techniques were employed to derive average and instantaneous turbulence intensity values. These measured values were incorporated as inlet boundary conditions in Computational fluid dynamics (CFD) simulations. The CFD analysis complements the experimental findings, providing insights into the physics of how the distorted turbulence field evolves when passing through the single-stage fan. A comparison with experimental data also highlights limitations in the unsteady Reynolds-averaged Navier-Stokes (RANS) model used. The results suggest that, in the presented test rig, changes in the loading of individual blades exert a more significant influence on turbulence field distortion downstream of the stage than the non-uniformity of inlet turbulent quantities. The average measured turbulence intensity between the rotor and the stator was 5.2%. Behind the stage, this value increased to 9.8% due to non-axisymmetric turbulence sources related to BLI in the stator row.

Keywords: boundary layer ingestion, turbulence, low speed fan, distorted inflow, BLI.

INTRODUCTION

Turbulence is defined as a three-dimensional time-dependent motion in which vortex stretching causes velocity fluctuations to spread to all wavelengths between a minimum determined by viscous forces and a maximum determined by the boundary conditions of the flow [1]. In the realm of turbomachinery, turbulence levels can significantly impact performance, particularly in low-speed machines operating at low Reynolds numbers. The location of the laminar-turbulent transition point on the suction surface of blades is highly dependent on flow conditions, especially the turbulence level [2]. Consequently, there is a keen interest in turbulence field measurements in axial fans and compressors. Acquiring quantitative data on turbulence is crucial for enhancing the accuracy of numerical simulations and understanding the physical phenomena occurring during the operation of specific turbomachinery components. A comprehensive understanding of turbulence is, therefore, vital for optimizing aircraft propulsors.

The literature provides valuable insights into turbulence in axial turbomachines, with a particular focus on compressors. Authors commonly detail experimentally measured turbulence levels,

occasionally including information on turbulence length scales. The reported turbulence intensity levels vary widely, influenced by factors such as inlet conditions, measuring section locations, and whether measurements pertain to blade wakes or the spaces between wakes. Notably, Wisler et al. [3] demonstrated that turbulence intensity in compressor blading wakes and endwall regions can reach up to 27%. However, values from other references cited in this section tend to be smaller, typically ranging from 3% to 12% for axial compressors. Schlichting and Das [4] discussed the impact of turbulence on transition and subsequent losses in cascades. Van Sintern [5] provided quantitative information about the increase in turbulence intensity after passing through multiple compressor stages. Meanwhile, Sharma [6] measured turbulence levels in a low-pressure turbine under sea level and cruising altitude conditions, highlighting the Reynolds number's influence on measured turbulence. Average turbulence intensities reported for a low-pressure turbine outlet were 12% at sea level and 15% at cruising altitude conditions, slightly higher than those for a typical axial compressor. Camp and Shin [2] presented a comprehensive analysis for multistage compressors, elucidating how turbulence intensities change in relation to flow and load coefficients, as well as turbulence length scales.

The mentioned studies focus on turbomachines operating in an undistorted axisymmetric flow. In contrast, this paper seeks to analyze the turbulence field within a low-speed fan test rig designed to simulate boundary layer ingestion (BLI) conditions in the inflow. This test stand was constructed as part of a project associated with the development of distortion-tolerant fan design methods, as detailed by Sieradzki et al. [7]

Boundary layer ingesting (BLI) fans hold significant promise for reducing fuel consumption in aircraft propulsion. According to Geiselhart et al. [8], the most fuel efficient configuration of an aircraft would be "a configuration with a partially buried engine, short offset diffuser using Active Flow Control, and a "D-shaped" inlet duct that ingests the boundary layer air". In BLI propulsion, fuel reduction is attributed to the reenergizing of the aircraft wake and improved propulsive efficiency, as discussed by Felder et al. [9, 10, 11] NASA's Generation-After Next (N+2) blended wing body (BWB) aircraft is set to incorporate an aft-mounted, airframe-embedded propulsion system capable of ingesting up to 16% of reduced velocity boundary layer air. Previous studies by Hardin et al. [12] have indicated a potential 3-5% reduction in fuel consumption compared to the undistorted, pylon-mounted baseline turbofans with an ultra-high bypass ratio. For N+3 generation aircraft, an even more substantial fuel burn reduction (on the order of 10%) is expected due to increased boundary layer air ingestion. However, the non-uniform and non-axisymmetric flow at the fan inlet poses a significant challenge for BLI propulsion. Research conducted at UTRC and NASA Glenn [13, 14] and at Whittle Laboratory [15, 16] has demonstrated that the highly distorted flow at the inlet leads to a decline in fan efficiency and a reduction in stall margin compared to non-distorted flow. Additionally, it results in alternating loading of the blades during one revolution, reducing the margin to the endurance limit of the rotor components, as shown by Bakhle et al. [17]

In the potential fan application, distortion is caused by the ingestion of a boundary layer from the aircraft fuselage. On the test stand, this distortion is introduced using a non-uniform porosity distortion screen located upstream of the rotor, designed according to the method described by Kwiatkowski et al. [18] The inlet-distorted total pressure profile used in both the experiment and CFD calculations is derived from the profile obtained in the Cambridge-MIT Institute Silent Aircraft project (SAX-40) [19, 20] and later utilized in the Whittle Laboratory Research Program [15]. This choice ensures a credible reproduction of realistic inflow conditions. It is important to note that the stand is equipped with a low-speed fan, which is not intended for use in powering aircraft. However, as demonstrated by Gunn and Hall [15], conclusions drawn from studies of low-speed BLI fans can generally be applied to high-speed BLI fans used in aerospace propulsion.

One of the challenges associated with boundary layer ingestion is the introduction of an increased and uneven turbulence intensity profile at the engine inlet. In the presented work, the distortion screen employed also introduces a non-uniform turbulence field in the inlet duct. The changes in this turbulence field after passing through the rotor and the stator of the single-stage fan are thoroughly analyzed and discussed. Another objective of the paper is to demonstrate the reliability of typical URANS-type simulations, commonly employed in the industry, with respect to modeling phenomena related to the generation and dissipation of turbulence in the given case.

METHODOLOGY

The low-speed fan test rig was designed and constructed to assess the performance characteristics of a fan with a non-uniform, non-axisymmetric inlet total pressure profile. The setup comprised a bellmouth inlet, followed by a 1.5 m inlet duct. The bellmouth was covered at the top with a plenum made of gauze-like fabric stretched around a lightweight aluminum frame. The plenum aimed to attenuate flow irregularities and reduce turbulence resulting from the limited laboratory volume. [21] In section 1, static pressure was measured using 8 circumferentially placed probes to estimate real-time air mass flow rate. The distortion screen was positioned over one diameter upstream of the rotor, followed by a flow straightener (honeycomb) to stabilize the distorted profile generated by the screen. The single-stage fan, with a diameter of 0.58 m, operated at a nominal rotational speed of 2500 RPM. The design flow and stage load coefficients were 0.5 and 0.47, respectively, for undistorted inlet flow conditions. The calculated average Reynolds numbers were 3.5×10^5 for the rotor (15 blades) and 1.2×10^5 for the stator (31 blades). The rotor blade tip clearance was designed to be 1 mm. However, during prolonged tests of the BLI case, the value measured by the light probe system was slightly lower (up to 0.8 mm) due to the high thermal expansion of the aluminum blades. This effect was thoroughly discussed in previous work [7] and was not considered in the simulation results presented later. The outlet section, containing 4 struts and approximately 1 m in length, was closed with a throttling cone to control the air mass flow rate. Both undistorted and distorted flow cases were tested at 8.16 kg/s, which corresponds to design point conditions for the undistorted case. A schematic of the test rig is depicted in Figure 1, highlighting all measurement sections, and presenting the distorted inlet total pressure profile. The azimuth angle convention used in the results discussion is also illustrated, with the angle measured from the lowest total pressure region counter-clockwise, aft looking forward. Turbulence measurements were conducted in sections 2–5. The analysis of the turbulence field was primarily based on experimental data, additionally supported by the results of CFD simulations.

INSTRUMENTATION

Turbulence level measurements were conducted using two independent single-sensor systems designed for the study of flow velocity and turbulence intensity. Each system consisted of a single Constant Temperature Anemometer (CTA) probe and a Dantec MiniCTA anemometer. The CTA measurement principle relies on maintaining a constant temperature of a thin flow-cooled wire. The heated wire element located at the probe tip is positioned in the flow field, where changes in air velocity lead to alterations in the wire resistance. Heat transfer from the wire is convective and depends on the flow velocity, the temperature difference between the wire and the air, as well as the physical attributes of the airflow. The sensor's stable temperature is maintained by a feedback control loop incorporating an electronic Wheatstone bridge circuit. Wisler et al. [3] noted that turbulence in a compressor stage is nearly isotropic, suggesting that single wire probes should offer sufficient accuracy for measurements. The Dantec probes, equipped with a tungsten wire of 5 µm in diameter and 1.2 mm in length, were utilized. It is crucial to note that a CTA system is highly sensitive to temperature oscillations. [22, 23]

For all measurements, the wires of CTA probes were fixed perpendicular to the main axis of the test

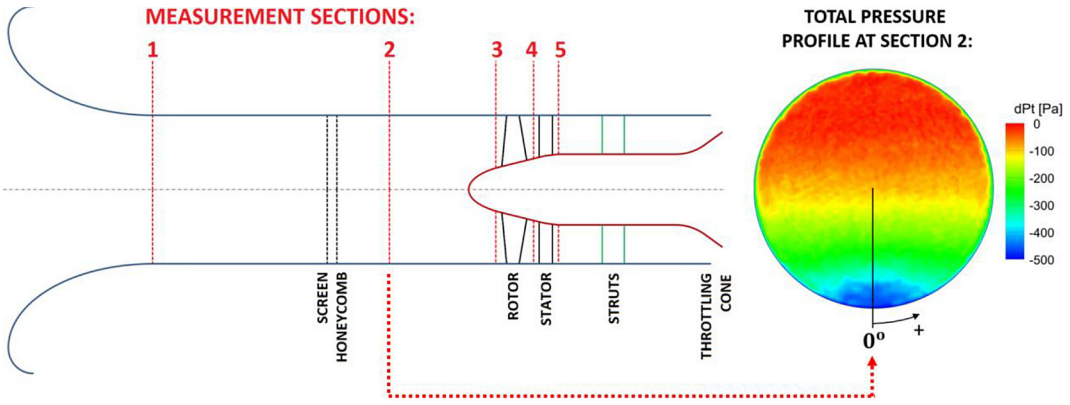

Figure 1. Schematic of the test rig and the distorted total pressure profile generated by the screen

rig, with the exception of section 4 where probe sensors were rotated 30 degrees, anticipating a high flow swirl angle in this section. The MiniCTA acquisition frequency was set to a relatively low value of 6 kHz due to the extended measurement times, up to 6 hours a day. Nevertheless, this value should allow for correct turbulence intensity measurement as the only considerations are that sufficient samples are taken to ensure statistical accuracy and that the sampling time is long compared to the period of the lowest frequency component of the signal [2]. The probes were mounted opposite to each other in an automatic traverse system, allowing radial movement into the flow (from the channel wall to the rotor axis) and rotation within the range of 180 degrees. Probe positions were determined based on the signal readout from two linear encoders and one angle encoder. To facilitate probe movement deep into the flow, the probes were equipped with 8 mm diameter steel extensions, ensuring a rigid mounting of probes and minimizing the potential for undesirable deflection and vibration. The traverse software used enabled the implementation of measurement maps and autonomous measurements. A depiction of the CTA probe mounted in the traverse system is presented in Figure 2.

EXPERIMENTAL DATA POSTPROCESSING

The temperature during calibration and the experimental test was measured by the EE310 temperature sensor with an accuracy of +/-0.2 °C. Due to the long-term measurement and the temperature difference between the calibration and proper measurement, a temperature correction was applied to obtain the corrected voltage E_{corr}:

$$E_{corr} = E_a \left(\frac{T_w - T_0}{T_w - T_a}\right)^{0.5} \quad (1)$$

where: E_a – acquired voltage, T_w – wire temperature, T_a – ambient temperature during the test, T_0 – ambient reference temperature during calibration. Output voltage obtained by CTA probes was transformed to the velocity V_{CTA} using King's equation:

$$V_{CTA} = (AE_{corr}^2 + B)^{1/n} \quad (2)$$

where: A, B, n – constants of the King's equation determined by calibration.

Data measured at sections located upstream of the rotor required only a typical calculation of turbulence intensity, based on the standard deviation of the local flow velocity and its mean value:

$$Tu = \frac{\sigma(V)}{\overline{V}} \quad (3)$$

where: Tu – turbulent intensity; V – flow velocity, m/s; $\overline{V}$ – mean flow velocity, m/s.

For measurement sections located downstream of the fan, it was necessary to filter out the rotor blade passing frequency and a number of its harmonics. This step was crucial as these frequencies are associated with repetitive flow unsteadiness (periodic fluctuations), not turbulence (chaotic fluctuations). The unsteadiness related to wakes could be observed at least two stages downstream from the stage of its origin. [24] This presents a significant challenge in processing turbulence parameters measured in turbomachinery. The primary goal was to eliminate the impact of rotor blade wakes on the measured level of turbulence. This objective was achieved through the use of Fourier Transformation of the signal and a Butterworth band-stop filter. Figure 3 illustrates

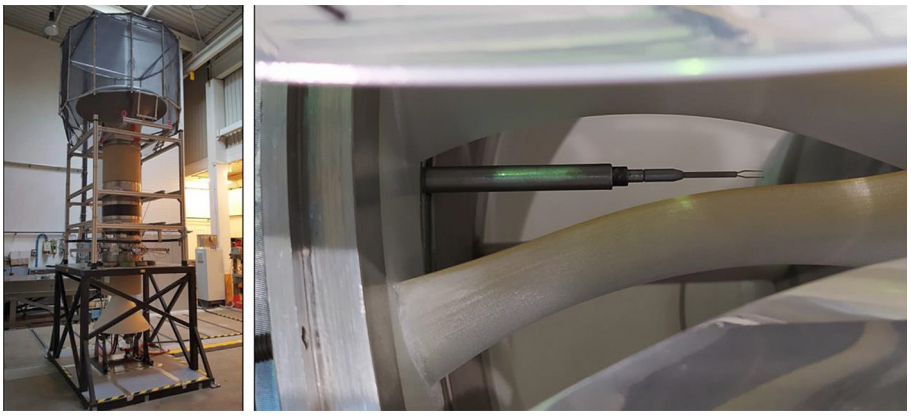

Figure 2. General view of the test rig and the hot-wire probe mounted in the traverse system

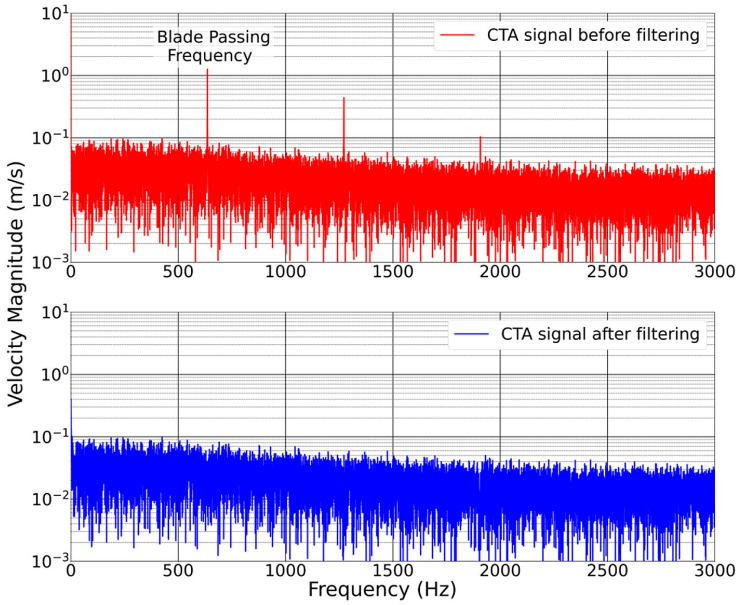

Figure 3. Spectrum of CTA velocity magnitude before and after frequency filtering (section 5 measurement)

an example of the CTA velocity spectrum before and after filtering.

Using this procedure, it was possible to determine only the average level of turbulence at a given point in space. The level of turbulence in the sections behind the rotor is highly variable, given that the rotating rotor blades traces have a much higher level of turbulence than the spaces between blades. To obtain comprehensive information about the level of turbulence at a given point and its changes, a specialized approach was required. One commonly used technique for this purpose, as employed by Evans [25] and Wisler et al. [3], is ensemble-averaging. However, this method necessitates the use of a blade passing trigger during measurements to capture many velocity traces locked to the same rotor position, also known as the phase-locked method. While a physical trigger of this kind was not utilized, similar results were achieved through additional CTA data postprocessing. Fourier Transformation of the original CTA probe signal enables precise determination of the blade passing frequency and interval for a given measurement point. CTA samples corresponding to the same blade-locked position (relative to the probe) were grouped to form a signal describing velocity fluctuations during a specific part of the blade passing period. This process was repeated for several blade-locked positions, each differing in the start time of the signal being created. It is important to note that this approach was applied only to individual points within the entire measurement map characterized by stable RPM. Analyzing the entire map using this method would be challenging due to changes in RPM during the test run, resulting from slight variations in the air temperature in the test room and the necessity to maintain the corrected RPM at a constant specified level.

NUMERICAL METHOD

Full-annulus unsteady Reynolds-averaged Navier–Stokes (URANS) simulations of the fan operating with distorted flow at the inlet were conducted. This kind of approach is currently considered as an industrial standard for turbomachinery components analyses. While URANS captures certain large-scale unsteady features, including rotor-stator interactions and periodic flow phenomena – some smaller structures may be under-resolved compared to more advanced techniques, such as large eddy simulations (LES) or direct numerical simulations (DNS). Consequently, unsteady flow phenomena influenced by finer-scale turbulence could be damped or not fully represented. Higher-fidelity turbulence-resolving methods (e.g., hybrid RANS-LES or wall-modeled LES) could provide more detailed insights into the turbulent flow structures but at a significantly higher computational cost.

To perform these simulations, the well-known commercial CFD solver FINE/Turbo was

employed, along with the k-ω shear stress transport (SST) turbulence model [26], an industrial standard in the field. The k–ω SST turbulence model is a two-equation eddy viscosity model combining the advantages of both k–ε formulation for free stream flow and k–ω formulations for boundary layers. However, these turbulence models still involve simplifying assumptions in their closure formulations. For example, the isotropic eddy viscosity assumption may not fully capture complex anisotropic turbulence, particularly in regions of highly three-dimensional flow structures or in the presence of separation. The Abu-Ghannam and Shaw (AGS) algebraic transition model [27] was used to predict laminar flow regions on the blades. The selection of the AGS model was based on its simplicity, low computational cost, and validated empiricism, as it was verified that a more sophisticated γ-Re model yields similar results in the undistorted axisymmetric case. However, the AGS model might also introduce uncertainty when predicting transition in flows with strong pressure gradients or where unsteady effects play significant role in flow. Although the presented results were verified against experimental data, caution should be used when generalizing these outcomes to other flow conditions or geometries where transition mechanisms differ noticeably.

The compressible flow model was applied with Merkle preconditioning activated due to the low subsonic Mach number regime. Spatial discretization employed the central scheme, while temporal discretization utilized an explicit four-stage Runge-Kutta scheme and a dual time-stepping technique [28]. The structural computational meshes of the multiblock O4H topology were generated using AutoGrid5/IGG meshing software, resulting in two grids with significantly different node counts (approximately 25 million and 86 million points). For both grids, the y+ values were maintained around 1. The coarse mesh was optimized for a balance between computational cost and solution accuracy in terms of the calculated stage efficiency value, making it suitable for optimization purposes. A grid dependency study indicated that further reduction of the node count noticeably affects the predicted performance of the fan, while an increase has little impact in this regard, as presented in Figure 4 The predicted stage efficiency drop due to BLI flow was also similar for the coarse and fine meshes, 1.25% and 1.23% respectively. Despite a relatively good prediction of stage performance in both undistorted and BLI conditions, the coarse mesh was not able to precisely capture all experimentally measured flow features in section 4 and 5. A detailed analysis of the influence of mesh density on the flow field was presented and compared with experimental data in one of the previous works [7]. The majority of the CFD results presented in this paper utilized the fine computational grid.

In summary, while the URANS-based framework with the k-ω SST and AGS models proved sufficiently accurate for predicting overall fan performance and capturing major flow features under inlet distortion, some modeling assumptions can theoretically limit the resolution of certain unsteady and small-scale turbulent processes. The results presented herein should be interpreted with these considerations in mind.

CFD BOUNDARY CONDITIONS DEFINITION

The inlet of the domain corresponds to section 2 of the test rig. At the inlet boundary condition, total pressure was specified using the

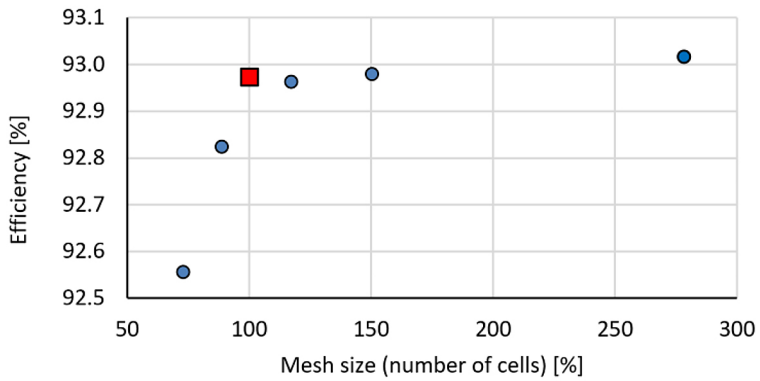

Figure 4. Grid dependence study (red square – coarse mesh)

experimentally measured profile (Fig. 1). A constant total inlet temperature was assumed. Turbulence intensity values, measured at section 2 by hot-wire probes, were also used during the specification of the inlet boundary condition. The turbulence kinetic energy k profile was calculated using the following equation:

$$k = \frac{3}{2}(\bar{V}Tu)^2 \tag{4}$$

The determination of the turbulence length scale, often identified as the average eddy size, although possible on the basis of hot-wire measurements and the autocorrelation function [2] or energy density spectrum [29], was performed in a different way. The reason for this decision was the low sampling frequency used, undermining the accuracy of the potential results obtained by these methods, but also striving to reproduce the correct turbulence dissipation rate in the CFD simulations. Numerical dissipation is also an important factor here, which would not be taken into account in the case of direct application of the measured turbulence length scales at the inlet boundary condition. The advantage of the method described below is that it naturally takes into account numerical dissipation and guarantees correct turbulence intensity decay. The turbulence length scale l can be easily converted to the turbulent dissipation rate ε used by the 2-equation turbulence model [30], according to the equation:

$$\varepsilon = \frac{C_\mu k^{3/2}}{l} \tag{5}$$

where: C_μ – turbulence model constant (0.09); k turbulent kinetic energy, m^2/s^2; l – turbulent length scale, m; ε – turbulent dissipation rate, m^2/s^3.

The appropriate size of the turbulence length scales was estimated to achieve the turbulence intensity values at section 3 consistent with the experiment. It was done iteratively, assuming that the turbulence length scale profile is a velocity-dependent quadratic function:

$$l(V) = l_{min} + \left(\frac{l_{max} - l_{min}}{V_{max} - V_{distorted}}\right)^2 (V_{max} - V)^2 \tag{6}$$

The lowest turbulence length scale value l_{min} corresponding to the highest (undistorted) velocity V_{max} in the discussed section. On the other hand, the highest value l_{max} was achieved for the velocity value $V_{distorted}$, connected with the region of distortion in the bottom part of the annulus. Additionally, the values of the turbulence length scale were limited near the walls, using the doubled distance of a given point from the wall as the maximum l value. The task was to find l_{min} and l_{max} values that guarantee good compliance with the experiment.

The measured velocity profile and final profiles of the inlet turbulence parameters are depicted in Figure 5. Section 2, situated almost one diameter upstream of the rotor, exhibited no significant unsteadiness or asymmetrical flow distortion due to fan operation. This permitted the use of a single probe measuring half of the section, while the second traverse could be employed for another quantity measurement. Consequently, the presented contour map of turbulence intensity is perfectly symmetrical, mirrored along the symmetry line. The obtained turbulence length scales demonstrated adequate turbulence dissipation, as illustrated in Figure 6. The changes in turbulence intensity upstream of the rotor are presented for two different CFD cases. In case a), the turbulence length scale profile defined by Eq. (6) was utilized, resulting in good compliance of the turbulence intensity field in section 3 with the experiment, both in the area of low and high flow velocities. Conversely, in case b), a uniform turbulence length scale profile

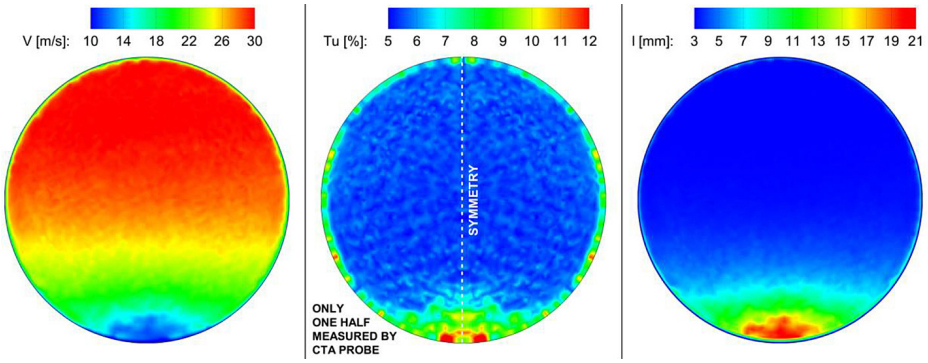

Figure 5. Contour maps of flow velocity and turbulence parameters in section 2

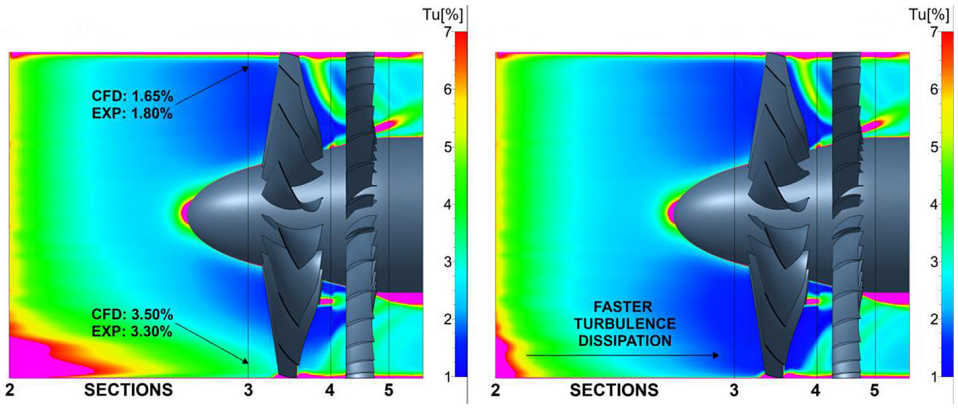

Figure 6. Calculated turbulence intensity changes upstream of the rotor with a) velocity-dependent and b) uniform turbulence length scale profiles at the inlet of the domain

(l = 3 mm) was applied, leading to a much faster dissipation of turbulence in the distortion region. Consequently, the operating conditions of the fan blades at azimuths close to 0° underwent noticeable changes due to the reduction in turbulence intensity from about 3.5% to 1.65%. This comparison emphasizes the importance of accurately defining the turbulence length scale at the domain's inlet, as it can substantially influence turbulence intensity levels, e.g. in the fan area.

It is also worth noting that the wall boundary condition in the CFD simulations assumed perfectly smooth surfaces for the rotor and stator blades, as well as the duct. This represents a simplification, as it neglects the impact of surface roughness, which could be particularly significant in the case of the duct composed of several superimposed ring sections and the stator, which was manufactured using 3D printing technology and smoothed with sandpaper.

The outlet was placed about 0.1 m downstream of the outlet guide vanes. The outlet boundary condition consisted of mass flow rate specification, based on the static pressure extrapolation and the velocity vector scaling technique.

RESULTS AND DISCUSSION

In the presented study, the fan was exposed to an uneven turbulence field with an increased turbulence level in the area associated with the distortion (Fig. 5). It is crucial to emphasize that the primary purpose of the distortion screen used was to accurately reproduce the total pressure profile distortion of the SAX-40 aircraft, not turbulence. While the obtained turbulence field may qualitatively resemble what could occur in such applications, it might not be entirely quantitative. This is particularly relevant for the turbulence length scale profile, as discussed in the preceding section of the paper.

Simple CFD analysis of a fully-developed turbulent boundary layer over a flat plate suggests that the maximum turbulence length scale size could reach about 50% of the boundary layer thickness. Considering the height of the distorted region and this observation, the scale of turbulence that could develop under real conditions might be approximately 10 times larger than what was obtained in the presented test rig case. In a real application, this could lead to a more uneven turbulence field directly in front of the fan, with less turbulence dissipation and potentially higher maximum turbulence intensity levels than generated by the distortion screen. However, it should be noted that other factors, such as the shape of the engine intake and flight conditions, may also significantly influence the formation of the inlet turbulence profile.

Comparison and discussion of the experimental and CFD results were conducted for sections 3, 4, and 5, with all contour maps presented in the aft looking forward convention. Additionally, the matrices of measurement points are displayed on the contour maps presenting the experimental data for sections 3 and 4. Measurements at these sections were performed on relatively low-resolution maps in the radial direction (9 radial positions), while section 5 was measured using a high-resolution map (36 radial positions), although not shown for the sake of clarity in the figure.

This work primarily focuses on the analysis of the turbulence field, while the comparison of experimental and CFD data for base flow parameters in all relevant sections is presented and discussed in the preceding paper [7].

Section 3 (in front of the rotor)

The analysis of experimental data in the first of the sections under consideration was relatively straightforward due to the low level of flow unsteadiness. Figure 7 presents a favorable comparison of the experimental and CFD data, which resulted from the accurate estimation of the inlet turbulence length scale profile in numerical simulations. In section 3, we can still identify the area of increased turbulence intensity connected with the low total pressure region, but the difference between the maximum and minimum values is notably smaller than in section 2. The areas of the highest turbulence intensity predicted by the CFD code near the shroud wall were not captured in the experiment due to the maximum radial position of the probe corresponding to 90% of the blade span. However, it is evident that at some points close to the shroud, the measured turbulence intensity is significantly higher than at neighboring points. This discrepancy is likely attributed to certain flow unsteadiness in the measurement room [21] and the fact that these points are located at the border of the area of increased turbulence. The sections near the hub and shroud wall, where measurements were not taken, were shown in all experimental contour maps to facilitate comparison with CFD results.

Section 4 (between the rotor and the stator)

The complexity of the flow field and the analysis required to obtain important information about turbulence is much greater in section 4, owing to the pronounced flow unsteadiness immediately behind the rotor. The results from section 4 are presented in Figure 8. A comparison of the experimental and CFD results for the averaged turbulence field (with the flow unsteadiness eliminated) reveals that in CFD, its level is underestimated at each point of the section. The most significant difference is observed near the hub and in the area containing point A, as marked in Fig. 8. The underestimated turbulence intensity near the hub is likely caused by the absence of modeling for the cavity between the rotor and the stationary part of the hub, as well as the lack of streamwise cavities between the individual platforms of the rotor blades in the CFD model. To identify the source of the difference for the region containing point A, spreading from azimuth -30°

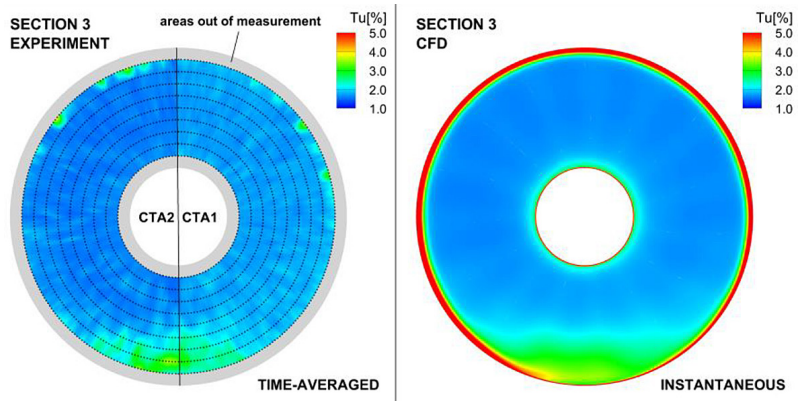

Figure 7. Contour maps of turbulence intensity at section 3 (experimental and fine grid CFD, aft-looking-forward convention)

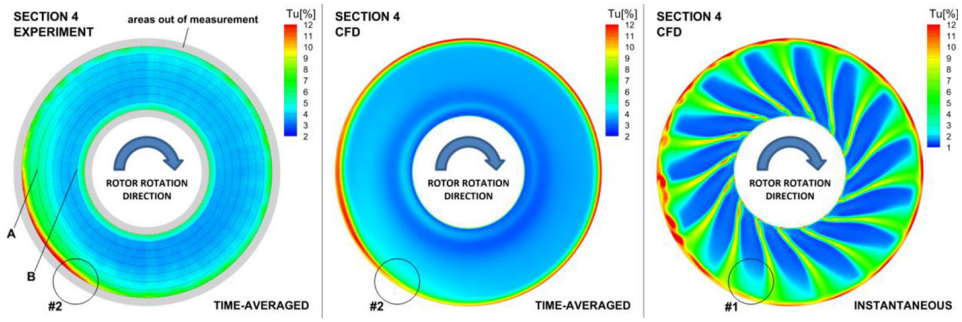

Figure 8. Contour maps of turbulence intensity at section 4 (experimental and fine grid CFD, aft-looking-forward convention)

to -130°, a thorough analysis of the turbulence intensity changes during the rotor blade passing period was conducted. The analysis was performed at two points (A and B) marked in Fig. 8, while Fig. 9 shows the results. It is evident that the level of background turbulence in the space between the blades is well predicted by CFD, with differences primarily appearing in the values measured in the blade wake. This discrepancy is attributed to the presence of numerical dissipation, contributing to faster turbulence decay, dependent, among other factors, on the density of the computational grid. The comparison of the turbulence dissipation rate in the rotor blade trace in two simulations differing in spatial and temporal resolution is shown in Figure 10. Simulations on the coarse grid were run using 10 time steps per blade passing period, while the fine grid computation used 50 time steps per blade passing period. Figures 8 and 9 clearly illustrate that achieving quantitative accuracy of the turbulence field in URANS simulations requires higher spatial and temporal resolutions than typically employed. Even the fine CFD simulation is burdened by excessive dissipation of highly turbulent rotor wakes. In Figure 9, the issue is more visible at 70% blade span due to the larger distance between the blade trailing edge and the measurement section than at 20% blade span.

Considering that the CFD simulation effectively reproduces the turbulence level for the bulk of the flow (between blades), it becomes possible to identify the impact of the ingested turbulence field distortion on the observed nonuniformity at section 4. For this purpose, the instantaneous field of turbulence intensity obtained numerically has been utilized. In Figure 8, area #1 is marked, showing an increase in turbulence intensity in the spaces between the blades, directly resulting from the ingested distorted turbulence field. As anticipated, it is shifted in the direction of rotation of the rotor due to a non-zero flow swirl angle behind the rotor, but it is characterized by only a slight increase in turbulence intensity. The contour of instantaneous *Tu* also confirms that point A is outside of this influence. The measured increase in turbulence in its vicinity cannot be attributed to the ingested turbulence field's nonuniformity, as no increase in turbulence can be observed between the blades at the azimuth -90°.

The instantaneous CFD results also indicate a full-span increase in *Tu* in the traces of the blades leaving the area of distortion (starting from azimuth corresponding to area #1) and significant turbulence production near the shroud for almost the same azimuths. This is clearly visible in both the time-averaged maps in CFD and in experimental data. The rotor blade passing through and leaving the distortion is characterized by the largest load due to a positive incidence angle. The incidence angle due to BLI represents the deviation of the inlet flow angle

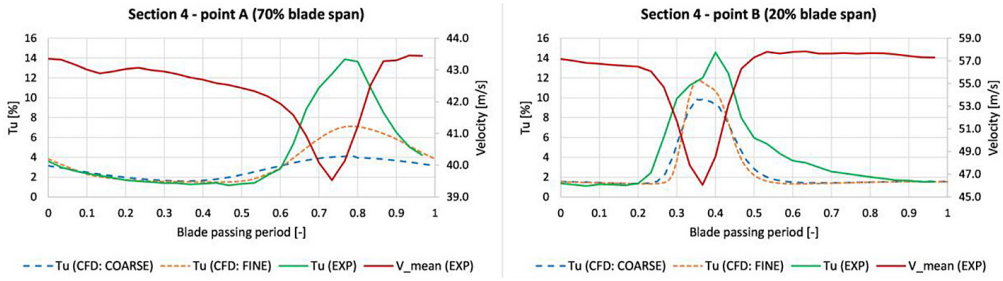

Figure 9. Line plots of turbulence intensity and mean velocity versus blade passing period at selected points of section 4

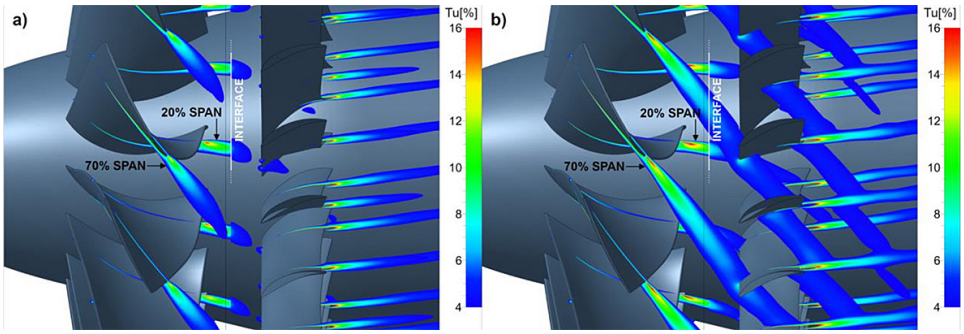

Figure 10. Comparison of wakes dissipation for a) coarse (25M points) and b) fine grid (86M points)

from the design value at axisymmetric flow and is shown in Figure 11. The largest rotor incidence angle can be observed on azimuths corresponding to the distorted flow region and near the shroud. This increases the level of turbulence in this area, especially around the tip of the blade exposed to the greatest load changes and more intense tip leakage vortex generation. It starts to become visible in both experimental and CFD time-averaged results at the same azimuth (marked with region #2 in Figure 8). It also perfectly matches the maximum blade load azimuth presented in Figure 12, which shows the circumferential variation of the integrated axial force acting on the blade in the BLI case with respect to the axisymmetric baseline case. In Figure 8, disorganized flow structures may be observed in the instantaneous *Tu* contour map for subsequent blade positions. The increase in *Tu* occurs with some delay relative to the region of positive rotor incidence, due to the flow swirl angle resulting from the operation of the rotor (rotor incidence angle is shown in section 3), and has a larger azimuthal spread because of the not immediate flow recovery around the blade.

The changes in rotor and stator incidence angles presented are caused by the axial velocity decrease in the region of the distortion and the flow redistribution upstream of the BLI fan. A detailed description of this phenomenon is available in the literature, as discussed by Gunn and Hall [15] and Sieradzki et al. [7], and is beyond the scope of this paper.

Section 5 (behind the stator)

The results for section 5 are also presented in the form of contour maps (Fig. 13) and line plots (Fig. 14). Line plots of turbulence intensity were generated for points C and D, which are marked in Figure 13. The findings indicate that the flow unsteadiness attributed to rotating rotor wakes is still observable but considerably less significant than in section 4. Simultaneously, there is a more constrained agreement between the results of CFD calculations and the experimental data within a narrower range of the blade passing period (Fig. 14). The simulations consistently underestimate the average turbulence level, primarily due to the lower turbulence intensity in the rotor blade wakes.

An analysis of turbulence intensity variation at points C and D reveals more pronounced

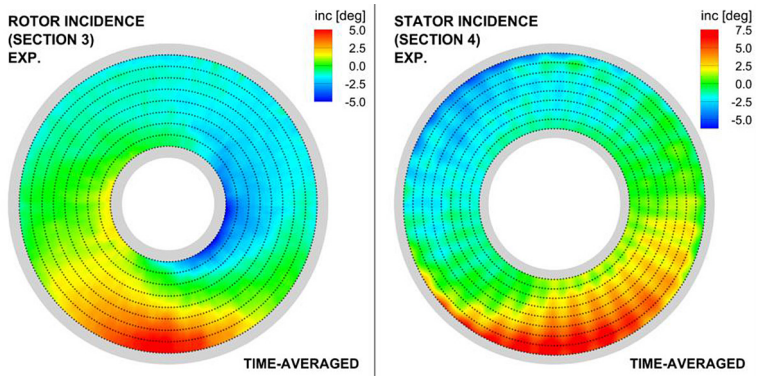

Figure 11. Contour maps of rotor and stator incidence angle (experimental data, aft-looking-forward convention)

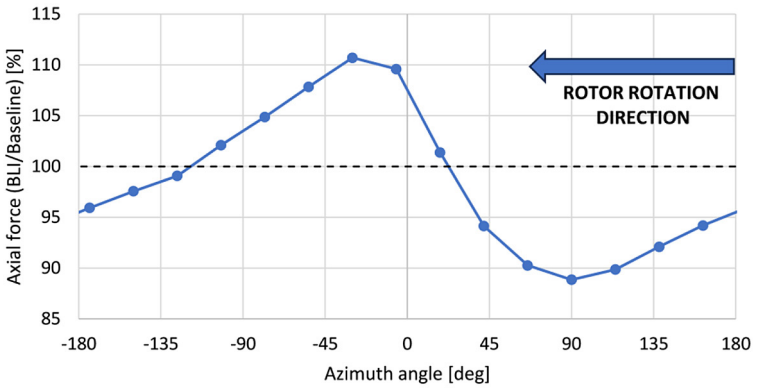

Figure 12. Plot of integrated axial force acting on blade versus azimuth angle (computational data)

turbulence changes in the experiment, ranging from 4 to 7 percentage points difference between the rotor blade traces and the lowest measured turbulence level. Conversely, the lowest values of turbulence intensity computed with CFD align well with the experiment (point C) or slightly overpredict (point D). The overprediction of the lowest turbulence intensities in CFD may result from excessive numerical dissipation, potentially unrealistically expanding the wakes' width and their influence on turbulence levels throughout the entire blade passing period.

It is noteworthy that the observed increase in the discrepancy between CFD and experimental data in section 5 is also associated with the presence of a grid interface between the rotor and the stator. As depicted in Figure 13, despite employing a fine computational grid and a relatively small time step, significant dissipation of the highly turbulent rotor blade wake remains visible at 20% of the blade span across the interface.

The increased turbulence level, clearly identified on negative azimuths in the experimental data from section 4, is also apparent in section 5. As anticipated, CFD simulation results do not reveal this region of increased *Tu* due to the reasons outlined in the preceding paragraph. Concurrently, the simulations accurately predicted new sources of non-axisymmetric turbulence in the stator row, situated near the hub at azimuths (-45°; 45°), near the shroud at azimuths (0°; 180°), and in the stator blade wakes at azimuths corresponding to positive stator incidence angles (Fig. 14). Similar to the rotor, these heavily loaded blades exhibit wider wakes and higher turbulence intensity in the wake. This aligns with the theory that the primary mechanism for turbulence creation in turbomachinery is wake generation (and wake chopping). Consequently, turbulence levels strongly correlate with wake thickness and, by extension, blade loading.

A summary of the experimentally measured values of turbulence intensity in sections 3, 4, and 5 is shown in Table 1. It can be observed

Table 1. Experimentally measured values of turbulence intensity

Section	Average *Tu*	Max. *Tu* in rotor blade wakes
3	1.9%	n/a
4	5.2%	~14%
5	9.8%	~9%

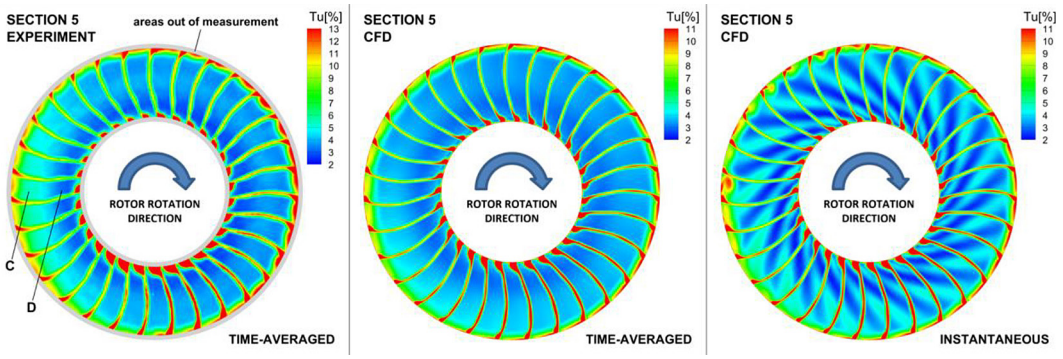

Figure 13. Contour maps of turbulence intensity at section 5 (experimental and fine grid CFD, aft-looking-forward convention)

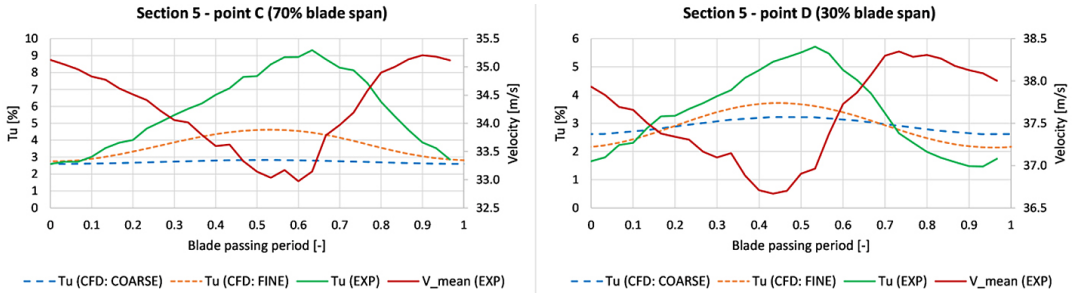

Figure 14. Line plots of turbulence intensity and mean velocity versus blade passing period at selected points of section 5

that the average *Tu* value almost doubles when transitioning from section 4 (behind the rotor) to section 5 (behind the stator). However, simultaneously, in the rotor blade wakes, the turbulence dissipates significantly. In the last section, the maximum value of *Tu* in the rotor blade wakes is even lower than the average *Tu* value for the entire section. This indicates a greater contribution of turbulence generated as a result of the flow around the stator blades.

The observed increase in turbulence levels resulting from BLI conditions can significantly impact the performance of an air-breathing machine. One key aspect to consider is the effect of turbulence on the position of the laminar-turbulent transition on the blade surfaces, which, in turn, influences blades' boundary layer thickness, wake width, and aerodynamic losses. In the case of a fan, the turbulence level in the incoming air is important; however, for subsequent blade rows, it is at least equally important to consider the turbulence generated by the upstream blade rows. As shown in the presented study, changes in blade loads resulting from the incidence angle are among the key factors shaping the turbulence field inside a BLI single-stage fan. It is also noteworthy that all turbulence kinetic energy, as described by Equation 4, generated during machine operation, should be considered a loss, as it ultimately dissipates into heat and cannot be recovered. Therefore, from an energy efficiency standpoint, the production of turbulent kinetic energy inside the machine should be minimized. This can be achieved by carefully designing stage geometry for BLI conditions, using e.g. non-axisymmetric stationary blade rows.

On the other hand, the turbulence levels inside an engine operating under BLI conditions are unlikely to have a significant impact on its durability, which is often a concern for BLI propulsors. This is because the load fluctuations caused by even increased turbulence levels are considerably smaller than those resulting from base flow distortion (illustrated in Fig. 12). However, under other operating conditions, turbulence could pose a threat to engine integrity – particularly in stall conditions, where strong flow instabilities occur. Stall margins, calculated with respect to the design point conditions, are often reduced for fans exposed to BLI flow [7, 16], highlighting the need for careful consideration during the design process.

CONCLUSIONS

Experimental measurements of turbulence intensity in a boundary layer ingesting (BLI) fan test rig have been presented and compared with the results of numerical simulations. The analysis of the collected data reveals the evolution of the initially distorted turbulence field after passing through a single-stage fan, leading to the formulation of the following observations and conclusions:

- In the presented case, the turbulence field distortion downstream of the stage is predominantly attributed to changes in the loading of individual blades due to BLI, rather than the distortion of the inlet turbulence field.
- This observation is case-specific because the distortion screen used did not permit the reproduction of realistic turbulence properties, especially the scale of turbulence. As a result, the initially distorted inlet turbulence field experienced intensified dissipation, leading to its relative homogeneity in the rotor blades' vicinity. Consequently, the impact of a non-uniform turbulence profile at the inlet is anticipated to be underestimated in the presented case. The adoption of alternative distortion generation methods is essential to obtain a more realistic turbulence profile.
- URANS numerical simulations, conducted with typical spatial and temporal resolution for general turbomachinery performance prediction, can offer valuable qualitative insights into turbulence generation mechanisms and sources. However, this computational approach is characterized by excessive turbulence dissipation, leading to an underestimation of predicted average turbulence levels. Achieving reliable predictions of turbulence intensity levels necessitates a less dissipative computational method.
- The experimentally measured average turbulence intensity between the rotor and the stator was approximately 5.2%, with maximum instantaneous values reaching 14% in the rotor blade wakes. Conversely, the average value measured behind the stage was 9.8%, accompanied by a reduction in the maximum value in the rotor blade wakes to about 9%. In the stator row, new sources of turbulence with a non-axisymmetric distribution contributed to a further increase in the mean turbulence level.

The scope of the research presented was inherently limited, leaving several questions unanswered. One of the key areas for future

investigation is the enhancement of experimental modeling of the turbulence field. While the distortion screen employed in this study successfully produced the desired velocity profile, it also intensified turbulence dissipation, as previously discussed. Modifying the honeycomb design or utilizing alternative turbulence generators – such as spikes with adjustable height and spacing or zig-zag turbulators on the vanes – could mitigate this limitation. Such improvements would enhance the study's credibility and enable broader generalization of the results.

Future work should also prioritize refining numerical turbulence modeling to achieve more accurate results in the blade wake regions, where the discrepancies between CFD simulations and experimental observations were most pronounced. Adopting higher-fidelity scale-resolved simulations, such as Stress-Blended Eddy Simulation (SBES) or Shielded Detached Eddy Simulation (SDES) [31], appears promising for capturing smaller structures in non-stationary flows. The test rig used in this study could facilitate the validation of turbulence models, particularly if the experimental setup is augmented with additional instrumentation to determine boundary layer transitions on the stator blades.

While these proposals focus primarily on improving turbulence modeling, expanding the range of operating conditions tested would also be advantageous. Future experiments could include other inlet velocity profiles and mass flow rates to provide a more comprehensive understanding of a fan performance under diverse conditions.

Finally, validating the results presented here using a higher-pressure-ratio fan would be a valuable undertaking. It is a challenge which would need a completely new setup with somehow similar approach. However, it seems achievable with designing a large flying aircraft model as a testbed and equipped with test setup, onboard logging devices or a telemetric systems. While defining and maintaining consistent test conditions would be demanding, this approach would more closely replicate real-world flow conditions, offering further insights into the practical applications of the research.

Acknowledgements

This research was conducted as part of the BLI-Fan research program, an outcome of the Polish-American partnership and collaboration between Łukasiewicz Research Network – Institute of Aviation and The Ohio State University. The authors wish to acknowledge the late Professor Meyer J. Benzakein, affiliated with The Ohio State University, for co-initiating this cooperation. The authors also express gratitude to the members of the BLI-Fan task group for their contributions and unwavering commitment to this research. The calculations were performed at the Academic Computer Centre in Gdańsk.

REFERENCES

1. Bradshaw, P. An Introduction to Turbulence and Its Measurement: Thermodynamics and Fluid Mechanics Series; Pergamon, Oxford, 1971.
2. Camp, T.R.; Shin, H.-W. Turbulence intensity and length scale measurements in multistage compressors. J. Turbomachinery 1995, 117, 1, 38-46. https://doi.org/10.1115/1.2835642
3. Wisler, D.C.; Bauer, R.C.; Okiishi, T.H. Secondary flow, turbulent diffusion, and mixing in axial-flow compressors. J. Turbomachinery 1987, 109, 4, 455–469. https://doi.org/10.1115/1.3262127
4. Schlichting, H.; Das, A. On the Influence of Turbulence Level on the Aerodynamic Losses of Axial Turbomachines. In Proceedings of the Symposium on Flow Research on Blading, Baden, Brown Boveri and Co. Ltd., 1970; 243–274.
5. Van Sintern, W. Investigation of the Velocity Flow Field and Rotor Loss Coefficient in an Embedded and Non-Embedded Rotor in a Low Speed Research Compressor Using Two-Dimensional X-Probe Hot Film Anemometry. Ph.D. Dissertation, RWTH Aachen University, Aachen, 1998.
6. Sharma, O. Impact of Reynolds Number on LP Turbine Performance. In Proceedings of the 1997 Minnowbrook II Workshop on Boundary Layer Transition in Turbomachines, Cleveland, Lewis Research Center, 1998; 65–70.
7. Sieradzki, A.; Kwiatkowski, T.; Turner, M.G.; Łukasik, B. Numerical modeling and design challenges of boundary layer ingesting fans. J. Turbomachinery 2022, 144, 11, 091007. https://doi.org/10.1115/1.4055265
8. Geiselhart, K.A.; Daggett, D.L.; Kawai, R.; Friedman, D. Blended Wing Body Systems Studies: Boundary Layer Ingestion Inlets With Active Flow Control. NASA, December 2003; NASA/CR-2003-212670. https://ntrs.nasa.gov/citations/20040031343.
9. Felder, J.L.; Kim, H.D.; Brown, G.V. Turboelectric Distributed Propulsion Engine Cycle Analysis for Hybrid-Wing-Body Aircraft. In Proceedings of 47th AIAA Aerospace Sciences Meeting, Orlando,

FL, January 2009; NASA. https://ntrs.nasa.gov/citations/20130010780

10. Felder, J.L.; Brown, G.V.; DaeKim, H.; Chu, J. Turboelectric Distributed Propulsion in a Hybrid Wing Body Aircraft. In Proceedings of 20th International Society for Airbreathing Engines, Gothenburg, September 2011; NASA. https://ntrs.nasa.gov/citations/20120000856
11. Felder, J.L.; Kim, H.D.; Brown, G.V.; Chu, J. An Examination of the Effect of Boundary Layer Ingestion on Turboelectric Distributed Propulsion Systems. In Proceedings of 49th AIAA Aerospace Sciences Meeting, Orlando, FL, January 2011; NASA. https://ntrs.nasa.gov/citations/20130010733
12. Hardin, L.; Tillman, G.; Sharma, O.; Berton, J.; Arend, D. Aircraft System Study of Boundary Layer Ingesting Propulsion. In Proceedings of 48th AIAA/ASME/SAE/ASEE Joint Propulsion Conference & Exhibit, July 2012. https://doi.org/10.2514/6.2012-3993
13. Florea, R.V.; Voytovych, D.; Tillman, G.; Stucky, M.; Shabbir, A.; Sharma, O.; Arend, D.J. Aerodynamic Analysis of a Boundary-Layer-Ingesting Distortion-Tolerant Fan. In Proceedings of the ASME Turbo Expo 2013: Turbine Technical Conference and Exposition, San Antonio, TX, June 2013. https://doi.org/10.1115/GT2013-94656
14. Arend, D.J.; Wolter, J.D.; Hirt, S.M.; Provenza, A.; Gazzaniga, J.A.; Cousins, W.T.; Hardin, L.W.; Sharma, O. Experimental Evaluation of an Embedded Boundary Layer Ingesting Propulsor for Highly Efficient Subsonic Cruise Aircraft. In Proceedings of 53rd AIAA/SAE/ASEE Joint Propulsion Conference, July 2017; American Institute of Aeronautics and Astronautics. https://doi.org/10.2514/6.2017-5041
15. Gunn, E.J.; Hall, C.A. Aerodynamics of Boundary Layer Ingesting Fans. In Proceedings of the ASME Turbo Expo 2014: Turbine Technical Conference and Exposition, Düsseldorf, Germany, September 2014. https://doi.org/10.1115/GT2014-26142
16. Perovic, D.; Hall, C.A.; Gunn, E.J. Stall inception in a boundary layer ingesting fan. J. Turbomachinery 2019, 141, 091007. https://doi.org/10.1115/1.4043644
17. Bakhle, M.A.; Reddy, T.S.; Coroneos, R.M. Forced Response Analysis of a Fan with Boundary Layer Inlet Distortion. In Proceedings of 50th AIAA/ASME/SAE/ASEE Joint Propulsion Conference, July 2014. https://doi.org/10.2514/6.2014-3734
18. Kwiatkowski, T.; Sieradzki, A.; Łukasik, B. Method of designing a distortion gauze for testing a boundary layer ingesting fan. Trans. Aerosp. Res. 2022, 1, 1-17. https://doi.org/10.2478/tar-2022-0001
19. Dowling, A.P.; Hynes, T. Towards a silent aircraft. Aeronaut. J. 2006, 110, 1110, 487–494. https://doi.org/10.1017/S000192400000138X
20. Madani, V.; Hynes, T. Boundary Layer Ingesting Intakes: Design and Optimization. In Proceedings of XIX International Symposium on Air Breathing Engines, Montreal, Canada, 2009; ISABE 1346.
21. Sieradzki, A.; Łukasik, B. Influence of the Limited Room Space on Inlet Conditions and Fan Operation at the Rotating Test Rig. J. Phys.: Conf. Ser. 2021, 1736, 012051. https://doi.org/10.1088/1742-6596/1736/1/012051
22. Jørgensen, F. How to Measure Turbulence with Hotwire Anemometers (A Practical Guide); Dantec Dynamics, Skovlunde, Denmark, 2002.
23. Lomas, C.G. Fundamentals of Hot Wire Anemometry; Cambridge University Press, 1986.
24. Cherrett, M.A.; Bryce, J.D. Unsteady viscous flow in a high-speed core compressor. J. Turbomachinery 1992, 114, 2, 287-294. https://doi.org/10.1115/1.2929142.
25. Evans, R.L. Some Turbulence and Unsteadiness Effects in Turbomachinery. In Turbulence in Internal Flows; Hemisphere Publishing Corp., Warrenton, 1977; 485–516.
26. Menter, F.R. Two-equation eddy-viscosity turbulence models for engineering applications. AIAA J. 1994, 32(8), 1598–1605. https://doi.org/10.2514/3.12149
27. Abu-Ghannam, B.J.; Shaw, R. Natural transition of boundary layers - The effects of turbulence, pressure gradient, and flow history. J. Mech. Eng. Sci. 1980, 22(5), 213–228. https://doi.org/10.1243/JMES_JOUR_1980_022_043_02
28. Jameson, A. Time Dependent Calculations Using Multigrid, with Applications to Unsteady Flows Past Airfoils and Wings. In Proceedings of Fluid Dynamics and Co-located Conferences, Honolulu, HI, June 1991; American Institute of Aeronautics and Astronautics. https://doi.org/10.2514/6.1991-1596
29. El-Gabry, L.A.; Thurman, D.R.; Poinsatte, P.E. Procedure for Determining Turbulence Length Scales Using Hotwire Anemometry. National Aeronautics and Space Administration, Glenn Research Center, Cleveland, 2014; NASA/TM-2014-218403
30. Wilcox, D.C. Turbulence modeling for CFD, 3rd Edition; DCW Industries: La Cañada, Calif, 2006.
31. Menter, F.R. Stress-blended eddy simulation (SBES) – A new paradigm in hybrid RANS-LES modeling. Notes on Numerical Fluid Mechanics and Multidisciplinary Design. 2018; 137, 27–37. https://doi.org/10.1007/978-3-319-70031-1_3